Acta Mech 209, 11–25 (2010)
DOI 10.1007/s00707-009-0150-y

Baozeng Yue · Dandan Yang

Study on the global chaotic dynamics and control of liquid-filled spacecraft with flexible appendage

Received: 19 November 2008 / Revised: 20 January 2009 / Published online: 5 March 2009

Abstract This paper investigates the global chaotic attitude dynamics and control of completely viscous liquid-filled spacecraft with flexible appendage. The focus in this paper is on the way in which the dynamics of the liquid and flexible appendage vibration are coupled. The equations of motion are derived and then transformed into a form suitable for the application of Melnikov's method. Melnikov's integral is used to predict the transversal intersections of the stable and unstable manifolds for the perturbed system. An analytical criterion for chaotic motion is derived in terms of the system parameters. This criterion is evaluated for its significance to the design of spacecraft. In addition, the Melnikov criterion is compared with numerical simulations of the system. Numerical solutions to these equations show that the attitude dynamics of liquid-filled flexible spacecraft possesses characteristics common to random, non-periodic solutions and chaos. This paper demonstrated that the desired final polarity control is guaranteed by using a pair of thruster impulses. The control strategy for a reorientation maneuver is designed and the numerical simulation results are presented for both the uncontrolled and controlled spin transition.

1 Introduction

The modern spacecraft often has a complicated structure consisting of a rigid platform, a fuel filled tank and some flexible appendages such as antennae reflectors or solar arrays [1–8]. Numerical results show that the motion of a torque-free spacecraft possesses characteristics common to random, non-periodic solutions due to the energy lost in fuel slosh and flexible appendage vibration. And this motion, for some sets of system parameters, was also theoretically proven, by using Melnikov's method, to be chaotic [1–6]. As such, the reorientation of the spacecraft relative to the inertially fixed angular momentum vector at the end of the maneuver cannot be determined a priori. More recently, Gray et al. have used Melnikov's method to detect the presence of chaotic dynamics originating from the saddles of damped satellites. The satellites were subject to small perturbations during an attitude transition maneuver, due to the presence of oscillating sub-masses, a flexible appendage limited to torsional vibrations, and a rotor immersed in a viscous fluid [1]. By employing Melnikov analytic and numerical methods, Yue studied the chaotic dynamics in an attitude transition maneuver of a rigid body with completely liquid-filled cavity in going from minor axis to major axis spin under the influence of viscous damping and small flexible appendages constrained to undergo only torsional vibration [3–5]. Considering the influence of aerodynamic drag and small structure damping, Yong and Tang investigated the chaotic dynamics of spacecraft with inside and outside vibrating attachments undergoing attitude maneuver from minor axis spin to major axis spin [6].

The determination and control of attitude evolution are important problems in modern spacecraft dynamics. In the case of single-body satellites, the problem of controlling the final orientation of the major axis has been

B. Yue (✉) · D. Yang
Department of Mechanics, School of Astronautics, Beijing Institute of Technology, 100081 Beijing, China
E-mail: bzyue@sohu.com

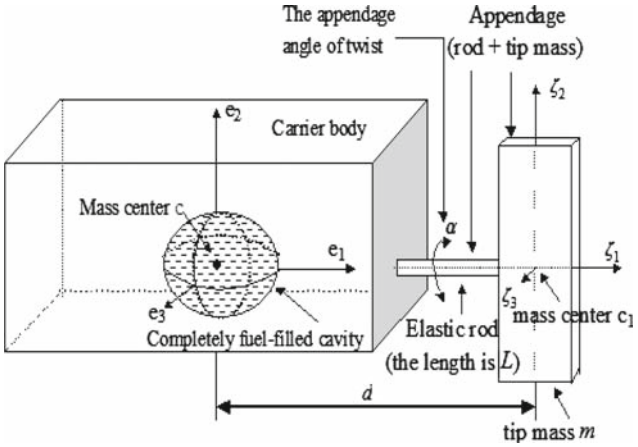

Fig. 1 The model of the liquid-filled spacecraft with flexible appendage

studied by many authors, such as Livneh et al. [9]. In terms of fuel usage, the passive spin transition maneuver is optimal, and momentum wheels, with their attendant complexity, are not required. To make the maneuver truly useful, however, the final spin polarity must be controlled, requiring some fuel expenditure. Rahn has modeled a spacecraft as a rigid body with a spherical, dissipative fuel slug, and found a control system that could guarantee any final orientation after the spin transition [10].

The chaotic attitude transition dynamics and control of the complicated spacecraft has not been solved in a form suitable for incorporation into attitude dynamics modeling. The goal of this paper is to investigate the chaotic attitude dynamics and to develop an attitude transition maneuver and guarantees a desired final orientation after spin transition for a completely viscous liquid-filled spacecraft with flexible appendage. In Sect. 2, we develop the mathematical equations and derive the Melnikov function using the residue theory. In Sect. 3, we obtain the conditions for the existence of transverse homoclinic points and discuss the bifurcation to Smale's Horseshoe. In Sect. 4, we turn to the chaotic attractors which are studied numerically. In Sect. 5, we develop the control strategy to obtain the desired final spin polarity. In Sect. 6, we conclude with a few remarks.

2 Mathematics formulations

2.1 Spacecraft model description

The spacecraft model considered (Fig. 1) is a system composed of a rigid carrier body b, with a completely liquid-filled spherical container and an elastic appendage a. This model is assumed to be free of any external moments such as gravity–gradient effects or atmospheric drag. An orthogonal coordinate frame e_1, e_2 and e_3 is attached to the center of mass of the entire system c. The carrier and liquid fuel have three components of the body angular momentum I_1, I_2, and I_3 about the major, intermediate, and minor body axes, respectively. The fuel is modeled as a spherical slug of inertia momentum J, which is surrounded by a viscous layer. The appendage a is modeled by a rigid-tip mass m joined to the carrier body by an elastic rod of length L and of negligible mass. The center of mass of the appendage a is located at c_1, a distance d along the e_1 axis. A second orthogonal coordinate frame ς_1, ς_2 and ς_3 is attached to the appendage at c_1 such that e_1 and ς_1 axes are collinear. For the appendage, the mass moment of inertia matrix with respect to the appendage coordinate frame ς_1, ς_2 and ς_3 is diag$\{A, B, C\}$. Next, quantities describing the motion of the model will be introduced. The relative rates between the spacecraft body and the fuel slug is designated as $\sigma_1, \sigma_2, \sigma_3$. The inertial angular velocity vector $\vec{\omega}$ of the carrier body b in the body-fixed reference frame is defined to be $\vec{\omega} = \omega_1\vec{e}_1 + \omega_2\vec{e}_2 + \omega_3\vec{e}_3$. The motion of the tip mass on the appendage is limited to rotation about the e_1 axis and is defined by the angle of twist α. No flexural bending or warping of the connecting rod is permitted. This type of motion is possible if, for example, the appendage is constrained by a system of guy wires [1,11]. As a result, motion of the appendage does not shift the center of the system. The connecting rod has a circular cross section and a torsional stiffness $K = SG/L$, where S is polar area moment of inertia, G is the shear modulus, and L is the length of the rod. The appendage can rotate at rate $\dot{\alpha}$ relative to the carrier body.

2.2 Equations of motion

The kinetic energy of the carrier body and the fuel slug is given by

$$T_1 = \frac{1}{2}\{(I_1 - J)\omega_1^2 + (I_2 - J)\omega_2^2 + (I_3 - J)\omega_3^2 + J[(\omega_1 + \sigma_1)^2 + (\omega_2 + \sigma_2)^2 + (\omega_3 + \sigma_3)^2]\}. \quad (1)$$

The inertia matrix of appendage is transformed so that its components are expressed in the body-fixed e_1, e_2 and e_3 frame instead of the appendage-fixed ς_1, ς_2 and ς_3 frame, and the kinetic energy is now derived to be

$$T_2 = \frac{1}{2}[A(\omega_1 + \dot{\alpha})^2 + B(\omega_2 \cos\alpha + \omega_3 \sin\alpha)^2 + C(\omega_3 \cos\alpha - \omega_2 \sin\alpha)^2 + md^2(\omega_2^2 + \omega_3^2)]. \quad (2)$$

The only component of the spacecraft that contributes to the potential energy is the torsional rod joining the carrier body to the tip mass of the appendage. This rod has torsional stiffness K, and thus, its potential energy is given by

$$V = \frac{1}{2}K\alpha^2. \quad (3)$$

The fully coupled nonlinear Lagrangian for flexible-liquid-spacecraft motion is

$$L = T_1 + T_2 + V. \quad (4)$$

By applying Lagrange's equation to the resulting form of Eq. (4), the familiar Newton-Euler angular momentum relationship is obtained:

$$\begin{aligned} \dot{h}_1 &= \omega_3 h_2 - \omega_2 h_3, \\ \dot{h}_2 &= \omega_1 h_3 - \omega_3 h_1, \\ \dot{h}_3 &= \omega_2 h_1 - \omega_1 h_2. \end{aligned} \quad (5)$$

Because the attitude dynamics of a torque free body, when measured in body angular momentum components, occur on the surface of the angular momentum sphere rather than ellipsoid as it is in body velocity components, we eliminate the angular velocity components by computing $\vec{h} = \{\partial L/\partial\vec{\omega}\}$ to get angular momentum components in terms of angular velocity components, where $\{\partial L/\partial\vec{\omega}\}$ is the gradient vector of the Lagrangian with respect to the angular velocities $\vec{\omega}$. And then we invert the resultant equations to solve for the angular velocity components in terms of the angular momentum components to obtain

$$\omega_1 = \frac{h_1 - A\dot{\alpha} - J\sigma_1}{I_1 + A}, \quad (6)$$

$$\omega_2 = \frac{1}{D_3}[2D_2h_2 - 2(B - C)h_3 \sin 2\alpha - 2D_2J\sigma_2 + 2J\sigma_3(B - C)\sin 2\alpha], \quad (7)$$

$$\omega_3 = \frac{1}{D_3}[2D_1h_3 - 2(B - C)h_2 \sin 2\alpha - 2D_1J\sigma_3 + 2J\sigma_2(B - C)\sin 2\alpha], \quad (8)$$

where D_1, D_2 and D_3 are, respectively, defined to be

$$D_1 = B + C + 2I_2 + 2md^2 + (B - C)\cos 2\alpha, \quad (9)$$

$$D_2 = B + C + 2I_3 + 2md^2 - (B - C)\cos 2\alpha, \quad (10)$$

$$D_3 = [(B - C)(\sin 2\alpha)]^2 - D_1D_2. \quad (11)$$

The complete equations of motion for the carrier body are given when we substitute Eqs. (6)–(8) into Eq. (5),

$$\dot{h}_1 = \frac{1}{D_3}\{2(D_1 - D_2)h_2h_3 - (h_3^2 - h_2^2)(B - C)\sin 2\alpha + [2J\sigma_2(B - C)\sin 2\alpha - 2D_1J\sigma_3]h_2 + [2D_2J\sigma_2 - 2J\sigma_3(B - C)\sin 2\alpha]h_3\}, \tag{12}$$

$$\dot{h}_2 = \frac{h_1h_3 - A\dot{\alpha}h_3 - J\sigma_1h_3}{I_1 + A} - \frac{1}{D_3}\{2D_1h_3h_1 - 2(B - C)h_2h_1\sin 2\alpha + [2J\sigma_2(B - C)\sin 2\alpha - 2D_1J\sigma_3]h_1\}, \tag{13}$$

$$\dot{h}_3 = \frac{h_1h_2 - A\dot{\alpha}h_2 - J\sigma_1h_2}{I_1 + A} + \frac{1}{D_3}\{2D_1h_2h_1 - 2(B - C)h_3h_1\sin 2\alpha + [2J\sigma_3(B - C)\sin 2\alpha - 2D_2J\sigma_2]h_1\}. \tag{14}$$

We now turn our attention to deriving the equation of motion for the flexible appendage. Rotation of the appendage relative to the carrier body is measured by the angle α, which is a generalized position coordinate of the system. The equation of motion for the appendage is given by the standard Lagrange's equation relationship

$$\frac{\mathrm{d}}{\mathrm{d}t}\frac{\partial L}{\partial \dot{\alpha}} - \frac{\partial L}{\partial \alpha} = 0. \tag{15}$$

Evaluating Eq. (15), we have the equation of motion for the appendage

$$A(\ddot{\alpha} + \dot{\omega}_1) - B(\omega_3\cos\alpha - \omega_2\sin\alpha)(\omega_2\cos\alpha + \omega_3\sin\alpha) + C(\omega_3\cos\alpha - \omega_2\sin\alpha)(\omega_2\cos\alpha + \omega_3\sin\alpha) + K\alpha = 0. \tag{16}$$

We use Eqs. (6)–(8) to substitute for ω_1, ω_2 and ω_3 in Eq. (16), noting that we must differentiate Eq. (6) to substitute for $\dot{\omega}_1$. From this we obtain the equation of motion for the appendage in terms of body angular momenta

$$\ddot{\alpha} = -\frac{(A + I_1)K\alpha}{AI_1} - \frac{\dot{h}_1 - J\dot{\sigma}_1}{I_1} + \frac{E(A + I_1)(B - C)}{AI_1D_3^2}, \tag{17}$$

where $\dot{h}_1$ is given by Eq. (12) and E is defined to be

$$\begin{aligned} E = {} & [(4B + 4I_2 + 4md^2)h_3\cos\alpha - (4B + 4I_3 + 4md^2)h_2\sin\alpha \\ & + (4B + 4I_3 + 4md^2)J\sigma_2\sin\alpha - (4B + 4I_2 + 4md^2)J\sigma_3\cos\alpha] \\ & \times [(4C + 4I_3 + 4md^2)h_2\cos\alpha + (4C + 4I_2 + 4md^2)h_3\sin\alpha \\ & - (4C + 4I_3 + 4md^2)J\sigma_2\cos\alpha - (4C + 4I_2 + 4md^2)J\sigma_3\sin\alpha]. \end{aligned} \tag{18}$$

In a similar way, the equations of motion for the fuel slug can be derived as

$$\dot{\sigma}_1 = \omega_3\sigma_2 - \omega_2\sigma_3 - \dot{\omega}_1 - \frac{\mu\sigma_1}{J}, \tag{19}$$

$$\dot{\sigma}_2 = \omega_1\sigma_3 - \omega_3\sigma_1 - \dot{\omega}_2 - \frac{\mu\sigma_2}{J}, \tag{20}$$

$$\dot{\sigma}_3 = \omega_2\sigma_1 - \omega_1\sigma_2 - \dot{\omega}_3 - \frac{\mu\sigma_3}{J}, \tag{21}$$

where μ is the viscous damping coefficient of the slug. Using Eqs. (6)–(8) to substitute for ω_1, ω_2 and ω_3 in Eqs. (19) and (20), we obtain the equation of motion for the fuel slug in terms of body angular momenta:

$$\begin{aligned}\dot{\sigma}_1 = \frac{1}{D_3}\{&[2D_1h_3\sigma_2 - 2(B-C)h_2\sigma_2\sin 2\alpha - 2D_1J\sigma_3\sigma_2 + 2J\sigma_2^2(B-C)\sin 2\alpha] \\ &- [2D_2h_2\sigma_3 - 2(B-C)h_3\sigma_3\sin 2\alpha - 2D_2J\sigma_3\sigma_2 + 2J\sigma_3^2(B-C)\sin 2\alpha]\} \\ &- \frac{\dot{h}_1 - A\ddot{\alpha} - J\dot{\sigma}_1}{I_1 + A} - \frac{\mu\sigma_1}{J}, \end{aligned} \tag{22}$$

$$\begin{aligned}\dot{\sigma}_2 = -\frac{1}{D_3}&[2D_1h_3\sigma_1 - 2(B-C)h_2\sigma_1\sin 2\alpha - 2D_1J\sigma_3\sigma_1 + 2J\sigma_2\sigma_1(B-C)\sin 2\alpha] \\ &+ \frac{\dot{h}_1 - A\dot{\alpha} - J\sigma_1}{I_1 + A}\sigma_3 - \frac{\dot{S}_1D_3 - S_1\dot{D}_3}{D_3^2} - \frac{\mu\sigma_2}{J}, \end{aligned} \tag{23}$$

$$\begin{aligned}\dot{\sigma}_3 = -\frac{1}{D_3}&[2D_2h_2\sigma_1 - 2(B-C)h_3\sigma_1\sin 2\alpha - 2D_2J\sigma_2\sigma_1 + 2J\sigma_3\sigma_1(B-C)\sin 2\alpha] \\ &+ \frac{\dot{h}_1 - A\dot{\alpha} - J\sigma_1}{I_1 + A}\sigma_2 - \frac{\dot{S}_2D_3 - S_2\dot{D}_3}{D_3^2} - \frac{\mu\sigma_3}{J}, \end{aligned} \tag{24}$$

where S_1 and S_2 are defined, respectively, as follows:

$$S_1 = 2D_2h_2 - 2(B-C)h_3\sin 2\alpha - 2D_1J\sigma_2 + 2J\sigma_3(B-C)\sin 2\alpha, \tag{25}$$

$$S_{21} = 2D_1h_3 - 2(B-C)h_2\sin 2\alpha - 2D_1J\sigma_3 + 2J\sigma_2(B-C)\sin 2\alpha. \tag{26}$$

Equations (12)–(14), (17) and (22)–(24) govern the dynamics of the overall system.

2.3 Nondimensionalization of the equations of motion

To apply Melnikov's method, we will introduce a small perturbation parameter ε and nondiensionalized Eqs. (12)–(14), (17), (22)–(24), and then transform them into a form consisting of an unperturbed part plus perturbation terms. To do this, we defined following scaled quantities:

$$\begin{array}{llll} \varepsilon = \dfrac{md^2}{I_2} & \tau = \frac{ht}{I_2} & \tilde{h}_i = \frac{h_i}{h} & \tilde{h}_i' = \left(\frac{I_2}{h^2}\right)\dot{h}_i \\ r_1 = \dfrac{I_3}{I_2} > 1 & r_2 = \frac{I_1}{I_2} < 1 & \tilde{\mu} = \frac{\mu}{h} & \tilde{\sigma}_i = \frac{I_2}{h\sqrt{\varepsilon}}\sigma_i \\ \tilde{\sigma}_i' = \dfrac{I_2^2}{h^2\sqrt{\varepsilon}}\dot{\sigma}_i & \tilde{\Omega} = \frac{\Omega I_2}{h} & r_3 = \frac{A}{B} & \tilde{J} = \frac{J}{I_2\sqrt{\varepsilon}} \\ \tilde{G}_1 = \dfrac{B}{md^2} & \tilde{G}_2 = \frac{C}{md^2} & \tilde{K} = \frac{KI_2}{h^2\varepsilon} & \frac{\mathrm{d}}{\mathrm{d}\tau} = \left(\frac{I_2}{h}\right)\frac{\mathrm{d}}{\mathrm{d}t} \end{array}$$

where $()' = \mathrm{d}()/\mathrm{d}\tau$ denote the differentiation with respect to non-dimensional time τ. We have assumed that $I_1 < I_2 < I_3$, therefore $0 < r_2 < 1 < r_1$. Notice that the number of moment of inertia parameters has been reduced to two r_1 and r_2. Carrying out the above change of variables leads to an equivalent set of dimensionless equations. These equations must be transformed into the aforementioned form consisting of an unperturbed part (found by discarding higher order terms, the unperturbed equations are just the equations for a torque-free rigid body) plus perturbed term in order to apply Melnikov's method. This is done by expanding the equations in powers of ε and keeping terms up to the appropriate order. The expanded equations can be written as

$$\tilde{h}_1' = [(1-r_1)/r_1]\tilde{h}_2\tilde{h}_3 + \varepsilon\{[(r_1^2-1)(G_1+G_2+2)/2r_1^2]\tilde{h}_2\tilde{h}_3/r_1^2 - \tilde{h}_2\tilde{J}\tilde{\sigma}_3/r_1 + \tilde{J}\tilde{h}_3\tilde{\sigma}_2\} + o(\varepsilon^2), \tag{27}$$

$$\tilde{h}_2' = [(r_1-r_2)(r_1r_2)]\tilde{h}_1\tilde{h}_3 + \varepsilon\{([(G_1+G_2+2)(r_2^2+2r_1r_2^2) - 2r_1^2G_1r_3)/2r_1^2r_2^2]\tilde{h}_1\tilde{h}_3 - G_1r_3\alpha'\tilde{h}_3/r_2 + \tilde{J}\tilde{h}_1\tilde{\sigma}_3/r_1 - \tilde{J}\tilde{\sigma}_1\tilde{h}_3/r_2\} + o(\varepsilon^2), \tag{28}$$

$$\tilde{h}_3' = [(r_2-1)/r_2]\tilde{h}_1\tilde{h}_2 + \varepsilon\{[(2r_1^2G_1r_3 - (G_1+G_2+2)(r_2^2+2r_1r_2^2))/2r_1^2r_2^2]\tilde{h}_1\tilde{h}_2 + G_1r_3\tilde{h}_2\alpha'/r_2 - \tilde{J}\tilde{h}_1\tilde{\sigma}_2 + \tilde{J}\tilde{\sigma}_1\tilde{h}_2/r_2\} + o(\varepsilon^2), \tag{29}$$

$$\alpha'' = -[\tilde{K}/(G_1r_3)]\alpha + [(r_1-1)/(r_1r_2)]\tilde{h}_2\tilde{h}_3 + o(\varepsilon), \tag{30}$$

$$(\sqrt{\varepsilon} - \varepsilon\tilde{J}/r_2)\tilde{\sigma}_1' = -\tilde{h}_1'/r_2 - \tilde{\mu}\tilde{\sigma}_1/\tilde{J} + \sqrt{\varepsilon}\tilde{h}_3\tilde{\sigma}_2/r_1 + \varepsilon[G_1r_3\alpha''/r_2 - G_1r_3\tilde{h}_1'/r_2] + o(\varepsilon^2), \tag{31}$$

$$(\sqrt{\varepsilon} - \varepsilon\tilde{J}/r1)\tilde{\sigma}_2' = -\tilde{h}_2' - \tilde{\mu}\tilde{\sigma}_2/\tilde{J} + \sqrt{\varepsilon}[-\tilde{h}_3\tilde{\sigma}_1/r_1 + \tilde{h}_1'\tilde{\sigma}_3/r_2] + \varepsilon[(G_1+G_2+2)\tilde{h}_2'/2] - \sqrt[3]{\varepsilon}(r_3G_1\alpha' + \tilde{J}\tilde{\sigma}_1)\tilde{\sigma}_3/r_2 + o(\varepsilon^2), \tag{32}$$

$$(\sqrt{\varepsilon} - \varepsilon\tilde{J}/r1)\tilde{\sigma}_3' = -\tilde{h}_3'/r_1 - \tilde{\mu}\tilde{\sigma}_3/\tilde{J} - \sqrt{\varepsilon}[\tilde{h}_2\tilde{\sigma}_1 + \tilde{h}_1'\tilde{\sigma}_2/r_2] - \varepsilon[(G_1+G_2+2)\tilde{h}_3'/2r_1^2] + \sqrt[3]{\varepsilon}(r_3G_1\alpha' + \tilde{J}\tilde{\sigma}_1)\tilde{\sigma}_2/r_2 + o(\varepsilon^2). \tag{33}$$

In the next section we describe a procedure to reduce Eqs. (27)–(33) to three equations, which have a spherical unperturbed phase space, by the elimination of Eqs. (30)–(33).

3 Melnikov method

3.1 Melnikov function

To apply Melnikov's method, the unperturbed phase space must have a structure that includes heteroclinic connections between pairs of saddle points or orbits homoclinic to a single saddle point. Melnikov's method will evaluate changes in the Poincaré map of this structure when the system is perturbed. The unperturbed phase space for the system given in Eqs. (27)–(33) is found by setting $\varepsilon = 0$. Doing so eliminates the dependence of Eqs. (27)–(29) on Eqs. (30)–(33) and allows us to solve Eqs. (27)–(29) independently of Eqs. (30)–(33). The unperturbed system of equations corresponding to Eqs. (27)–(29) are given by

$$\tilde{h}_1' = \frac{1-r_1}{r_1}\tilde{h}_2\tilde{h}_3, \tag{34}$$

$$\tilde{h}_2' = \frac{r_1-r_2}{r_2r_1}\tilde{h}_1\tilde{h}_3, \tag{35}$$

$$\tilde{h}_3' = \frac{r_2-1}{r_2}\tilde{h}_1\tilde{h}_2, \tag{36}$$

and are identical to Euler's rotational equations of motion for a torque-free rigid body. The phase space for the unperturbed system is a sphere shown in Fig. 2, where the non-dimensional body-fixed angular momentum components $\tilde{h}_1$, $\tilde{h}_2$ and $\tilde{h}_3$ are the phase variables. The phase space has six equilibrium points at $\{(\pm1, 0, 0), (0, \pm1, 0), (0, 0, \pm1)\}$ where the equilibrium points $(\pm1, 0, 0)$ and $(0, 0, \pm1)$ are neutrally stable centers corresponding to minor and major axis spin, respectively, and the equilibrium points at $(0, \pm1, 0)$ are unstable hyperbolic saddle points corresponding to intermediate axis spin. Note the presence of heteroclinic orbits jointing the pair of saddle points.

Melnikov's method is now applied to the system of equations (27)–(33). Melnikov's method is a perturbation technique that gives global information about the system's dynamics. The method detects intersections of the stable and unstable manifolds of hyperbolic saddles in planar Poincaré maps. Existence of these intersections implies the existence of Smale horseshoes and chaos via the Smale-Birkhoff theorem (see [12]). For a detailed presentation of Melnikov theory, see Guckenheimer and Holmes or Wiggins (see [12–14]). The most common version of Melnikov's method considers systems of the form

$$\vec{x} = \vec{f}(\vec{x};\vec{\beta}) + \varepsilon\vec{g}(\vec{x},\tau;\vec{\beta}), \qquad \vec{x} = \begin{Bmatrix} u \\ v \end{Bmatrix} \in R^2, \tag{37}$$

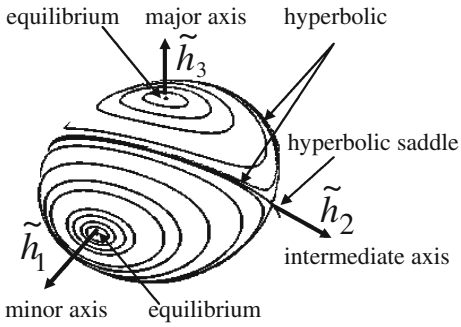

Fig. 2 Momentum sphere illustrating the heteroclinic orbits and the hyperbolic saddle points, curves are orbits of constant energy

where $\vec{g}$ is periodic in τ, $\vec{f}(\vec{x}, \vec{\beta})$ is a Hamiltonian vector field defined on R^2, and $\varepsilon\vec{g}(\vec{x}, \tau, \vec{\beta})$ is a small perturbation, which need not be Hamiltonian. $\vec{x} = (\tilde{h}_1, \tilde{h}_2, \tilde{h}_3, \alpha, \alpha', \tilde{\sigma}_1, \tilde{\sigma}_2, \tilde{\sigma}_3)$, and $\vec{\beta}$ is a vector of system parameters. It would appear that Melnikov's method would not be applicable to a system given the form of the equations in Eq. (37). That is, Melnikov's method applies to systems whose Poincaré map is planar and the system considered herein is eight-dimensional. On the other hand, close inspection of Eqs. (27)–(33) reveals that Eqs. (30)–(33) couple with Eqs. (27)–(29) only through the perturbation terms in Eqs. (27)–(29). Therefore, we can solve Eqs. (27)–(29) for their unperturbed solutions, that is, the solutions for $\tilde{h}_1$, $\tilde{h}_2$ and $\tilde{h}_3$ with $\varepsilon = 0$, and substitute these solutions into Eqs. (30)–(33). We then solve Eqs. (30)–(33) for their unperturbed solutions, that is, the solution for α, $\tilde{\sigma}_1$, $\tilde{\sigma}_2$ and $\tilde{\sigma}_3$, with $\varepsilon = 0$, and then substitute the unperturbed solutions for α, $\tilde{\sigma}_1$, $\tilde{\sigma}_2$ and $\tilde{\sigma}_3$ into the perturbations of Eqs. (27)–(29). This process results in three non-autonomous equations in $\tilde{h}_1$, $\tilde{h}_2$ and $\tilde{h}_3$, with the unperturbed parts represented by Euler's equation of rotational motion, and perturbation terms which are functions of the $\tilde{h}_i$, the system parameters, and time τ. This process of reducing our system to three first-order equations from eight still does not admit the application of the planar form of Melnikov's method. However, a result due to Holmes and Marsden (see [1]) allows us to apply Melnikov's method directly to the equations involving $\tilde{h}_1$, $\tilde{h}_2$ and $\tilde{h}_3$. The Melnikov function, as given in [1], can be written as

$$M(\tau_0) = \int_{-\infty}^{\infty} \nabla\tilde{h}[\vec{q}_0(\tau)] \times \{\vec{f}[\vec{q}_0(\tau)] + \vec{g}[\vec{q}_0(\tau), \tau + \tau_0]\}\mathrm{d}\tau, \tag{38}$$

where $\nabla\tilde{h}$ is the gradient of the Hamiltonian $\tilde{h}$ of the unperturbed system with respect to $\tilde{h}_i$, $\vec{f}$ is the unperturbed part of the system, $\vec{g}$ is the $O(\varepsilon)$ perturbation of the system, and $\vec{q}_0(\tau)$ is the solution for the heteroclinic orbits or trajectories of the unperturbed system. The non-dimensional Hamiltonian for the system is given by $\tilde{h} = \frac{1}{2}(\tilde{h}_1^2/r_2 + \tilde{h}_2^2 + \tilde{h}_3^2/r_1)$ and is simply the kinetic energy of the unperturbed system, that is, of the carrier body. The gradient of $\tilde{h}$ with respect to the body-fixed angular momentum components is, thus, the vector $\nabla\tilde{h} = \{\tilde{h}_1/r_2,\ \overleftrightarrow{h}_2,\ \tilde{h}_3/r_1\}$. Because it can be readily shown that $\nabla\tilde{H} \times f = 0$, Eq. (38) simplifies to

$$M(\tau_0) = \int_{-\infty}^{\infty} \nabla\tilde{H}[\vec{q}_0(\tau)] \times \vec{g}[q_0(\tau), \tau + \tau_0]\mathrm{d}\tau. \tag{39}$$

Before the integral in Eq. (39) can be evaluated, we must find the solutions $\vec{q}_0(\tau)$along the heteroclinic orbits of the unperturbed system given by Eqs. (34)–(36), and find the unperturbed solution to Eqs. (30)–(33) so that we may substitute for α', $\tilde{\sigma}_i$ into the perturbation terms of Eqs. (27)–(29).

The solution along the heteroclinic orbits can be found in terms of hyperbolic trigonometric functions (see [1]). These solutions are given as follows:

$$\tilde{h}_1 = s_1 X_1 \,\mathrm{sech}(\mathrm{d}\tau), \tag{40}$$

$$\tilde{h}_2 = s_2 \tanh(\mathrm{d}\tau), \tag{41}$$

$$\tilde{h}_3 = s_3 X_3 \,\mathrm{sech}(\mathrm{d}\tau), \tag{42}$$

where $X_1 \triangleq \sqrt{r_2(1-r_1)/(r_2-r_1)}$, $X_3 \triangleq \sqrt{r_1(r_2-1)/(r_2-r_1)}$, $\mathrm{d} \triangleq \sqrt{(r_1-1)(1-r_2)/(r_1 r_2)}$, and s_1, s_2, s_3 are each ± 1 and are chosen such that the product $s_1 s_2 s_3 = 1$ (these permutations give all four of the heteroclinic orbits shown in Fig. 2).

We can solve Eqs. (31)–(33), with $\varepsilon = 0$, for $\tilde{\sigma}_i$ by substituting in the unperturbed solutions for $\tilde{h}_i'$:

$$\tilde{\sigma}_1 = -\frac{\tilde{J}\tilde{h}_1'}{r_2\tilde{\mu}}, \tag{43}$$

$$\tilde{\sigma}_2 = -\frac{\tilde{J}\tilde{h}_2'}{\tilde{\mu}}, \tag{44}$$

$$\tilde{\sigma}_3 = -\frac{\tilde{J}\tilde{h}_3'}{r_1\tilde{\mu}}. \tag{45}$$

We can solve Eq. (30), with $\varepsilon = 0$, for α by substituting in the unperturbed solutions for $\tilde{h}_2$ and $\tilde{h}_3$. The approximate solution to this equation is derived by Gray et al. [1] to be $\alpha = A\sin(\Omega\tau + \Phi)$, where the square of the amplitude A is given by

$$A^2 = \left[\alpha_0 - \frac{\pi C}{2d^2}\sec\frac{\pi\Omega}{2d}\right]^2 + \left\{\frac{\alpha_0'}{\Omega} + \frac{C}{\Omega d} + \frac{C}{2d^2}\left[\pi\tanh\frac{\pi\Omega}{2d} + i\Psi\left(\frac{d+i\Omega}{4d}\right) - i\Psi\left(\frac{d-i\Omega}{4d}\right)\right]\right\}^2, \tag{46}$$

the tangent of the phase angle Φ is given by

$$\tan\Phi = \left[\alpha_0 - \frac{\pi C}{2d^2}\sec\mathrm{h}\frac{\pi\Omega}{2d}\right] \Big/ \left\{\frac{\alpha_0'}{\Omega} + \frac{C}{\Omega d} + \frac{C}{2d^2}\left[\pi\tanh\frac{\pi\Omega}{2d} + i\Psi\left(\frac{d+i\Omega}{4d}\right) - i\Psi\left(\frac{d-i\Omega}{4d}\right)\right]\right\}, \tag{47}$$

where α_0 is the initial angle of twist of the torsional appendage, α_0' is the initial twist rate, Ω is the frequency of the appendage oscillation defined by $\Omega \triangleq \sqrt{\tilde{K}/(\lambda G_1 r_3)}$ and $\lambda = md^2/(ml^2)$. C is defined by

$$C \triangleq \frac{r_1 - 1}{r_1 r_2}\sqrt{\frac{r_1(1-r_2)}{r_1 - r_2}}. \tag{48}$$

And $\Psi = \Psi(z)$ is Euler's digamma function defined for complex variables as follows:

$$\Psi(z) = \int_0^\infty \left[e^{-\tau} - \frac{1}{(1+\tau)^z}\right]\frac{\mathrm{d}\tau}{\tau}, \qquad R(z) > 0. \tag{49}$$

In accordance with Melnikov's method, we now replace τ by $\tau + \tau_0$ everywhere that τ appears explicitly. We then substitute the resulting expression for $\tilde{\sigma}_i$ and α' into Eqs. (27)–(29) to obtain the final form of the Melnikov integration.

The Melnikov integral given in Eq. (39) is now expanded, and the unperturbed solutions (Eqs. (40)–(42)), along the heteroclinic orbits, are substituted for $\tilde{h}_1$, $\tilde{h}_2$ and $\tilde{h}_3$ in the integral. Because the integral is performed over the interval $(-\infty, \infty)$, all odd functions in the integrand can be eliminated leaving the following terms in the Melnikov integral:

$$\begin{aligned} M(\tau_0) = {} & \int_{-\infty}^{\infty} [2G_1\lambda r_3\left(\frac{1}{r_2} - \frac{1}{r_1 r_2}\right) X_3 A\tilde{\Omega}\tanh(\mathrm{d}\tau) \times \sec\mathrm{h}(\mathrm{d}\tau) \times \sin(\Omega\tau) \times \sin(\tilde{\Omega}\tau_0 + \Phi)]\mathrm{d}\tau \\ & -2\int_{-\infty}^{+\infty} X_1 X_3 \tilde{J}^2 \mathrm{d}\left[\left(\frac{1}{r_1^2 r_2\tilde{\mu}} - \frac{1}{r_1^2\tilde{\mu}}\right)(\sec\mathrm{h}\mathrm{d}\tau)^2(\tanh\mathrm{d}\tau)^2 - \left(\frac{1}{r_1\tilde{\mu}} - \frac{1}{r_2\tilde{\mu}}\right)(\sec\mathrm{h}\mathrm{d}\tau)^4\right]\mathrm{d}\tau. \end{aligned} \tag{50}$$

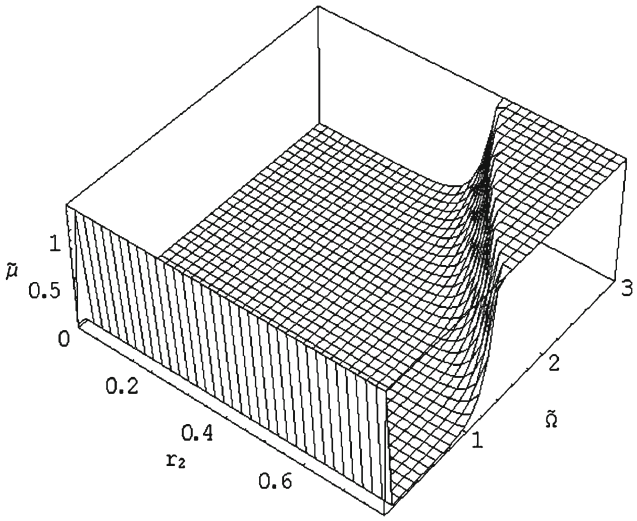

Fig. 3 Surface separating chaotic from non-chaotic motion

The integrals in Eq. (50) can be evaluated symbolically with software Mathematica (see [15]). After integrating, we arrive at the Melnikkov function for our system of equations:

$$M(\tau_0) = G_1 r_3 \frac{r_2 - 1}{r_1 r_2} A\Omega^2 \frac{\pi}{d} \operatorname{sech} \frac{\pi \Omega}{2d} \sin(\Omega\tau_0 + \Phi) - \left[\frac{r_2(1-r_1)}{r_2 - r_1}\right]^{\frac{1}{2}} \times \left[\frac{4(r_2 - r_1)\tilde{J}^2}{3r_1 r_2 \tilde{\mu}} - \frac{2(1-r_2)\tilde{J}^2}{3r_1^2 r_2 \tilde{\mu}}\right]. \tag{51}$$

Because the Melnikov function is a measure of distance between stable and unstable manifolds in the Poincaré map of our system, zeros of the Melnikov function indicate intersections of the two manifolds. The function contains two terms, one of which is constant and the other one varies sinusoidally with τ_0. Zeros of this function will occur wherever the amplitude of the sinusoidal terms is greater than the constant term. The Melnikov criterion becomes

$$G_1 r_3 \frac{r_2 - 1}{r_1 r_2} A\Omega^2 \frac{\pi}{d} \operatorname{sech} \frac{\pi \Omega}{2d} \geq \left[\frac{r_2(1-r_1)}{r_2 - r_1}\right]^{\frac{1}{2}} \left[\frac{4(r_2 - r_1)\tilde{J}^2}{3r_1 r_2 \tilde{\mu}} - \frac{2(1-r_2)\tilde{J}^2}{3r_1^2 r_2 \tilde{\mu}}\right]. \tag{52}$$

This criterion is valid provided that the perturbation parameter ε is sufficiently small.

3.2 Results based on Melnikov's method

We have analytically proven the existence of chaos in the attitude motion of an energy dissipating, completely liquid-filled satellite with flexible appendage. The derived criterion can be used to find chaotic and non-chaotic region in parameter space and, if necessary, avoid chaotic motion in this class of satellite systems. Inspection of Eq. (52) reveals that the Melnikov criteria are a function of 8 of the 12 non-dimensional system parameters $(r_1, r_2, r_3, \tilde{K}, \tilde{\Omega}, G_1, \tilde{J}, \tilde{\mu})$. If we satisfy Eq. (52) and the aforementioned restriction on the carrier body's shape parameter r_1 and r_2 (where $0 < r_2 < 1 < r_1 < 1 + r_2$), then the system, modeled by Eqs. (27)–(33), exhibits chaotic dynamics near the unperturbed heteroclinic orbits for sufficiently small ε. By fixing five of the parameters, the others can be studied in a three-dimension parameter space. Parametric studies of three-dimension parameter subspace for Eq. (52) are shown in Figs. 3 and 4.

Figure 3 shows the dividing surface between chaotic and non-chaotic motion in $r_2 - \tilde{\Omega} - \tilde{\mu}$ space as determined by Eq. (52). The movement of inertia parameters were chosen to be $r_1 = 1.1$, $r_3 = 3.0$, $\tilde{J} = 0.8$, $G_1 = 0.5$. Values of the parameters above the surface are chaotic. It can be seen that the dependence of the criterion for chaos on the shape of the rigid body is apparent. The surface "flattens" out at $\tilde{\mu} = 1$ since we

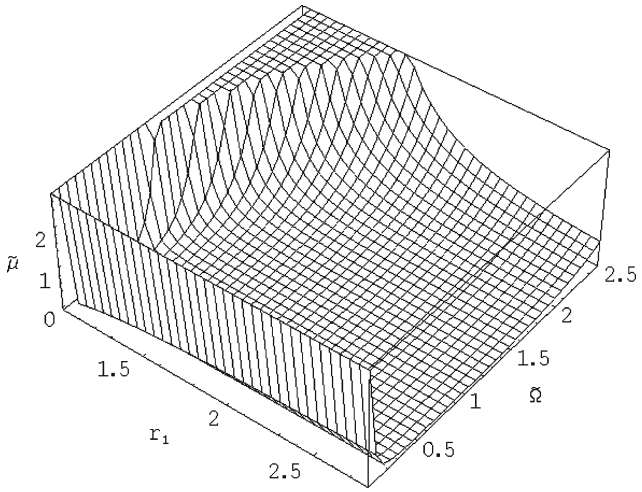

Fig. 4 Surface separating chaotic from non-chaotic motion

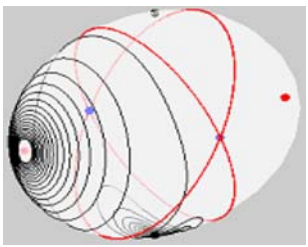

Fig. 5 The path of the angular velocity vector in body axis coordinates starts with a positive minor axis spin and finishes with negative major axis spin

impose $\tilde{\mu}$ <1. We can see that as $r_2 \to 1$, chaotic motion is impossible to obtain for any value of $\tilde{\mu}$ and $\tilde{\Omega}$. This shape corresponds to a nearly symmetric oblate carrier body.

Figure 4 shows the dividing surface between chaotic and non-chaotic motion in $r_1 - \tilde{\Omega} - \tilde{\mu}$ space as determined by Eq. (52). The movement of inertia parameters were chosen to be $r_2 = 0.7$, $r_3 = 1.0$, $\tilde{J} = 0.2$, $G_1 = 0.1$. The surface shows the dependence of the criterion for chaos on the shape of the rigid body. We see that for values of $r_1 \to 1$, which corresponds to a nearly symmetric prolate body, no chaotic motion occurs. As $\tilde{\Omega} \to 0$, no chaotic motion occurs since a zero forcing frequency implies no perturbation.

4 Numerical simulation

In case of no external forcing movement, the viscous fuel slug provides the energy dissipation. T decreases and the energy ellipsoid shrinks with time. This leads to an open polhode path that spirals outward from the minor axis, and captures on the major axes, as shown in Figs. 5 and 6, which is obtained by simulating Eqs. (27)–(33) with the initial conditions $y_0 = [\cos(\pi/36), \sin(\pi/36), 0, 0, 0, 0, 0, 0, 0]$; the values of parameters used in numerical simulating can be found in Table 1. As shown clearly in Figs. 5 and 6, the orientation of the spacecraft relative to the inertially fixed angular momentum vector at the end of the maneuver cannot be determined a priori. The final polarity is sensitive to the value changes of the system parameters. The spacecraft can end up with either a positive or a negative major axis spin. Physically, this corresponds to two final attitudes that are 180° apart.

Figures 7, 8 and 9 are obtained by simulating Eqs. (27)–(33) with the initial conditions $y_0 = [\cos(\pi/36), \sin(\pi/36), 0, 0, 0.0, 0.0, 0.0, 0.0, 0]$; the values of system parameters used to generate these figures can also be found in Table 1. In all figures in this section, the "long" axis corresponding to the minor axis and that the trajectory starts at the left pole (positive minor axis).

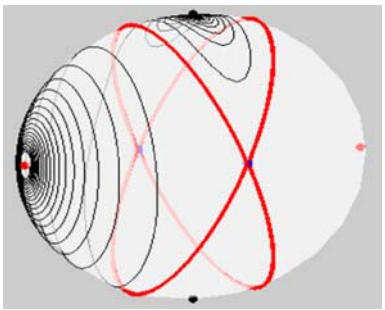

Fig. 6 The path of the angular momentum vector in body axis coordinates starts with a positive minor axis spin and finishes with positive major axis spin

Table 1 Parameters used in Figs. 5–9 to generate trajectories

Parameters	r_1	r_2	r_3	$G_1 = G_2$	$\tilde{K}$	$\tilde{J}$	$\tilde{\mu}$	$\tilde{\Omega}$
Major axis spin, Fig. 5	1.10	0.80	1.00	0.10	3.50	0.80	0.02	1.12
Major axis spin, Fig. 6	1.10	0.60	1.10	0.10	2.50	0.10	0.15	1.60
Period-1 spin, Fig. 7	1.10	0.80	1.50	0.50	0.10	0.80	0.15	0.92
Period-2 spin, Fig. 8	1.50	0.65	1.50	0.80	0.50	0.80	0.65	0.44
Chaotic, Fig. 9	1.10	0.75	3.00	0.50	0.10	0.80	0.15	0.26

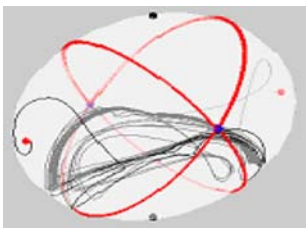

Fig. 7 The path of the angular velocity vector in body axis coordinates starts with a positive minor axis spin and finishes with negative major axis period-1 spin

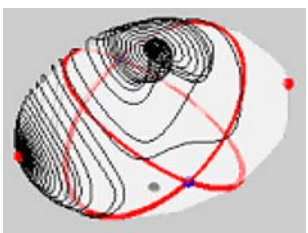

Fig. 8 The path of the angular velocity vector in body axis coordinates starts with a positive minor axis spin and finishes with positive major axis period-2 spin

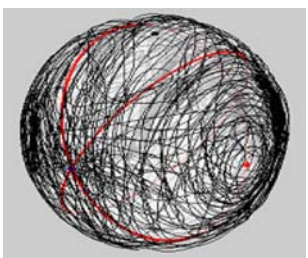

Fig. 9 The path of the angular velocity vector in body axis coordinates starts with a positive minor axis spin and finishes with chaotic spin

Because of the high dimension of the parameter space, it is a tough task to get a thorough investigation of the nonlinear behavior of the complex system modeled as that in Sect. 2.1. From the numerical results presented in this paper, it is seen that the attitude dynamics of a liquid-filled spacecraft with a flexible appendage can exhibit some unusual behaviors such as limit cycles, period-n limit cycles, quasi periodic trajectories and chaotic trajectories. The simulations shown in Figs. 5, 6, 7, 8 and 9 are only a small, though representative, sample of the total number of simulations we performed in order to understand the behavior of the complex spacecraft modeled as that in Sect. 2.1 in this paper. Checking through all data used in producing Figs. 5, 6, 7, 8 and 9 showed that, with few exceptions, Melnikov's method bounds those regions of parameter space leading to chaotic dynamics. We also found that in most cases, the Melnikov criterion also bounds those regions of parameter space possessing period-n limit cycles and quasi-periodic trajectories, excluding the trajectories presented in Figs. 7 and 8 that represent the case of limit cycles or period-2 trajectories.

5 Control strategy and its implementation

Many spacecraft have sensitive onboard instruments which must be shielded from the sun, or directioned communication equipment which must point toward the Earth. In these cases, it is desirable to ensure a final spin polarity. This paper presents a control system that guarantees a final orientation after spin transition. For brevity, we only take into account one case of the spin transitions in the previous section, i.e., the case in Fig. 5. The desired final spin polarity is guaranteed with the following control strategy. Initially, the spacecraft spins about its minor axis with some small amount of nutation. The spacecraft begins to transit to flat spin, and when the polhode crosses the separatrix the spin direction is determined according to the sign of rate changes. If the spin direction is correct, no action is taken. If the spin direction is incorrect, a thruster is fired to force the polhode to cross the separatrix. Then, a short time later, an opposite thruster is fired, causing the polhode to recross the separatrix on the desired side. In this section, we drop the tildes of the parameters for convenience. The distance between the polhode and the separatrix is measured by the characteristic parameter [10]

$$I = h^2/2T \quad (I_1 \le I \le I_3). \tag{53}$$

As the energy of the body decreases, I increases. When the polhode is at the separatrix crossing, $I = I_2$. The characteristic parameter qualitatively divides the motion into a regime of primarily minor axis spin ($I < I_2$) and primarily major axis spin ($I > I_2$). Defining K as the equivalent gain of the thruster firing,

$$I^+ = KI, \tag{54}$$

where I^+ is the characteristic parameter after the firing. If $I < I_2$, and the objective of the firing is to cross the separatrix, then K is chosen > 1 such that $I^+ > I_2$. This is called an in-cross firing because the firing moves the polhode across the separatrix in the same direction as energy dissipation. For a separatrix crossing in the opposite direction (out-cross), K is chosen < 1. The equivalent gain is calculated from the thruster impulses i_1, i_2 and i_3 by assuming that the thruster firings are impulsive [10]:

$$K = \frac{h^2 + 2(h_1 i_1 + h_2 i_2 + h_3 i_3) + i_1^2 + i_2^2 + i_3^2}{h^2 + 2[(I_2/I_1)h_1 i_1 + h_2 i_2 + (I_2/I_3)h_3 i_3] + (I_2/I_1)i_1^2 + i_2^2 + (I_2/I_3)i_3^2}. \tag{55}$$

For most practical cases, an impulse about the minor axis that is fired when $\omega_2 = 0$ uses the least propellant for a given K. The size of the thruster impulse can be calculated by substituting $\omega_2 = 0$, $i_3 = 0$ and $i_2 = 0$ into Eq. (55) and solving for i_1:

$$i_1 = -h_1 + \mathrm{sgn}(h_1)\sqrt{h_1^2 - \frac{I_1 h^2 (1 - K)}{I_1 - K I_2}}. \tag{56}$$

Designating Δt as the time from $\omega_1 = 0$ to $\omega_2 = 0$, the worst case I at the first thruster firing would be

$$I = I_2 + 3\Delta t \left(\frac{\partial I}{\partial t}\right)_{\text{Separatrix}} \tag{57}$$

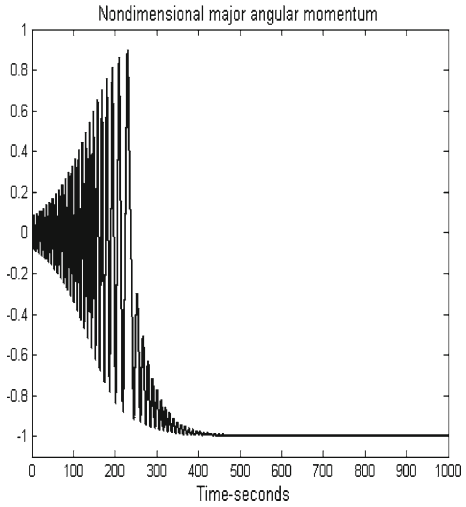

Fig. 10 Time response of major angular momentum

The desired I^+ should be large enough to ensure the separatrix is not in-crossed before $\omega_1 = 0$ a quarter period later, or

$$I = I_2 - \Delta t \left(\frac{\partial I}{\partial t}\right)_{\text{Separatrix}} \tag{58}$$

Substituting Eqs. (57) and (58) into Eq. (54) and utilizing Eq. (53) yields

$$K = \frac{1 + \Delta t[(1/T)(\partial T/\partial t)]_{\text{Separatrix}}}{1 - 3\Delta t[(1/T)(\partial T/\partial t)]_{\text{Separatrix}}}. \tag{59}$$

Numerical simulation results are presented in Figs. 10–13. Figure 10 shows the simulated time response of the major angular momentum for the completely viscous liquid-filled spacecraft with flexible appendage under the same initial condition as in Fig. 5. Figure 11 shows the simulated controlled time response of the major angular momentum under the same initial condition as in Fig. 5. Figure 12 shows the polhode path with spin polarity control strategy under the same initial condition as in Fig. 5. The trajectory is shown on the surface of the momentum sphere in $h_1 - h_2 - h_3$ space, and the two great circles passing through the h_2 axis are the unperturbed heteroclinic orbits. Figure 13 shows the simulated polhode path for a controlled spin transition with the same initial conditions as in Fig. 5. The control system is configured to ensure a positive final spin angular momentum. The polhode first crosses the separatrix at point 1. When h_1 is zero (point 2), h_3 will be less than zero. When h_2 crosses zero (point 3), a thruster is fired and the polhode out-crosses the separatrix at point 4. Next, h_3 crosses zero (point 5), signaling successful completion of the separatrix crossing. At point 6, h_2 crosses zero, the second thruster is fired and the polhode recross the separatrix on the desired side (for comparison between Figs. 12 and 13, all the switch points are marked on the polhode in Fig. 13, while only points 3, point 4 and point 6 are marked on the polhode in Fig. 12).

6 Conclusions

In this paper, the eight-dimensional ordinary differential equations governing the attitude motion of the completely liquid-filled spacecraft with flexible appendage are derived and transformed into the form suitable for the application of Melnikov's method. By using the Melnikov integral, we obtain the theoretical criteria of the chaotic attitude motion of the spacecraft. In addition, subspace of the full-parameter space are studied analytically and numerically to obtain a qualitative and quantitative understanding of the interaction of the various parameters leading to nonlinear motion. From the analytical results, it is shown that the shape of the rigid body and forcing frequency have profound influence on the onset of chaotic dynamics of an energy dissipating, completely liquid-filled spacecraft with flexible appendage. From the numerical results, it is seen that the perturbed completely liquid-filled satellite possesses not only many random characteristics of

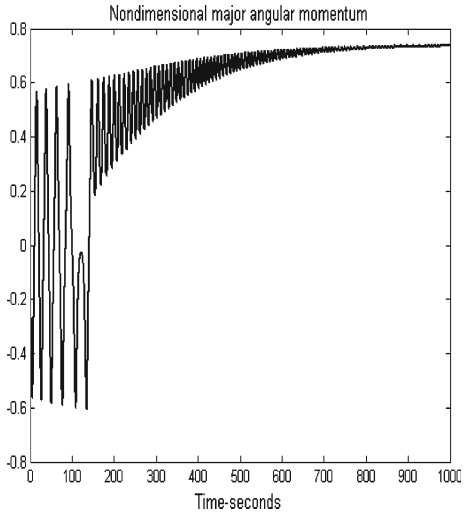

Fig. 11 Controlled time response of major angular momentum

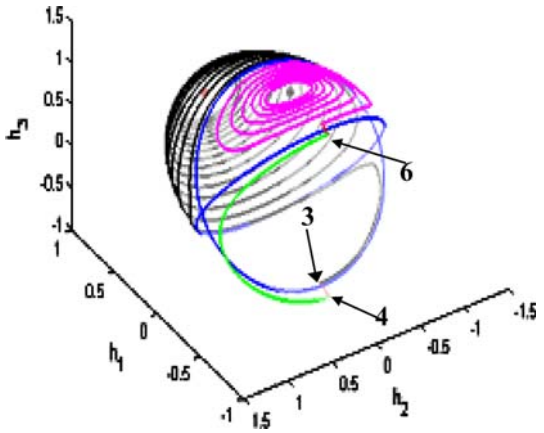

Fig. 12 Polhode path simulation with spin polarity control

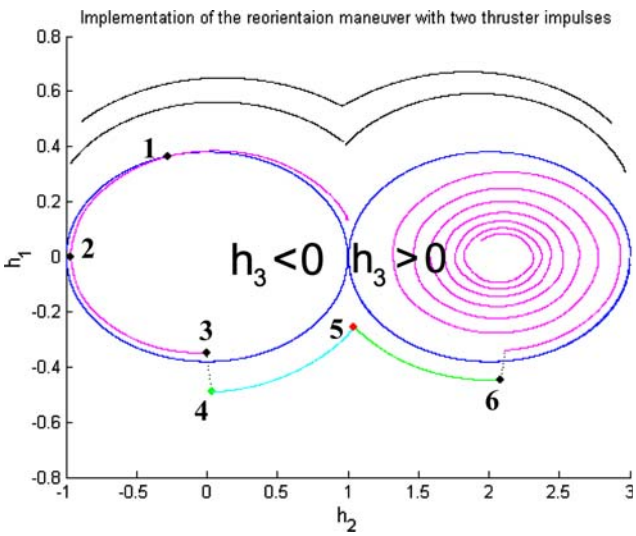

Fig. 13 Polhode path simulation with spin polarity control. The polhode plot is projected on a plane showing both the positive and negative final polarity regions

a non-periodic solution which are theoretically proved to be chaotic by using the Menikov's method, but also possesses many other unusual behaviors such as period-n trajectories and quasi periodic trajectories which can also be predicted by Melnikov's method. This paper shows that the desired reorientation maneuver can be acquired by using a pair of thruster impulses. The control strategy for the reorientation maneuver is designed and the control strategy utilizes rate sign changes to determine when the separatrix has been crossed and when the impulse must be switch on. The size of the impulses is calculated based on estimates of the energy dissipation in the spacecraft. The numerical simulation results are presented for both the uncontrolled and controlled spins transition.

Acknowledgments This project is supported by Natural Science Foundation of China (Nos. 10572022, 10772026), Ph. D. Programs Foundation of Ministry of Education of China (No. 200800070011), Scientific Research Foundation of Ministry of Education of China for Returned Scholars (20080732040) and Program of Beijing Municipal Key Discipline Construction.

References

1. Miller, A.J., Gray, G.L.: Nonlinear spacecraft dynamics with a flexible appendage damping, and moving internal submasses. J. Guidance Control Dyn. **24**, 605–615 (2001)
2. Meehan, P.A., Asokanthan, S.F.: An analysis of chaotic instabilities in a rotating body internal energy dissipation. Int. J. Bifurcation Chaos **16**, 1–19 (2006)
3. Yue, B.: Heteroclinic bifurcations in completely liquid-filled spacecraft with flexible appendage. Nonlinear Dyn. **51**, 317–327 (2008)
4. Yue, B.: Chaotic attitude maneuvers in spacecraft with a completely liquid-filled cavity. J. Sound Vib. **302**, 643–656 (2007)
5. Yue, B.: Chaotic dynamics of liquid-filled flexible spacecraft in the large angle attitude maneuver. Chin. J. Theor. Appl. Mech. **40**, 388–393 (in Chinese) (2008)
6. Yong, E., Tang, G.: Chaotic attitude motion of a spacecraft under periodic perturbation. J. Astronaut. **26**, 535–540 (in Chinese) (2005)
7. Lü, J., Li, J., Wang, T., Yue, B.: Nonlinear dynamics analysis of a liquid-filled spacecraft with elastic appendages. J. Tsinghua Univ. **47**, 27–33 (in Chinese) (2007)
8. Peng, D., Xu, S., Jing, W.: Variable structure control of flexible liquid-filled spacecraft. J. Harbin Inst. Technol. **35**, 1196–1198 (in Chinese) (2003)
9. Livneh, R., Wie, B.: Asymmetric body spinning motion with energy dissipation and constant body-fixed torques. J. Guidance Control Dyn. **22**, 322–328 (1999)
10. Rahn, C.D., Barba, P.M.: Reorientation maneuver for spinning spacecraft. J. Guidance Control Dyn. **14**, 724–728 (1991)
11. Mazzoleni, A.P., Hall, C.D., Stabb, M.C.: Double averaging approach to the study of spin up dynamics of flexible satellites. J. Guidance Control Dyn. **19**, 54–59 (1996)
12. Guckenheimer, J., Holmes, P.: Nonlinear Oscillations, Dynamical Systems, and Bifurcations of Vector Fields, Sects. 4.5, 5.3. Springer, New York (1983)
13. Wiggins, S.: Global Bifurcations and Chaos, Chap. 4. Springer, New York (1988)
14. Wiggins, S.: Introduction to Applied Nonlinear Dynamical Systems and Chaos, Sect. 4.5. Springer, New York (1990)
15. Wolfram, S.: The Mathematica Book, Sect. 3.5, 4th edn. Cambridge University Press, New York (1999)